Effects of thermal ageing and ion irradiation on intergranular P segregation in low alloy steel welds

Leifeng Zhang, Bertrand Radiguet, Patrick Todeschini, Christophe Domain, Yang Shen, Philippe Pareige

Effects of thermal ageing and ion irradiation on intergranular P segregation in low alloy steel welds

Leifeng Zhang [a,b,*], Bertrand Radiguet [a], Patrick Todeschini [c], Christophe Domain [c], Yang Shen [d], Philippe Pareige [a]

[a] Groupe de Physique des Matériaux, UMR CNRS 6634, Université de Rouen Normandie et INSA de Rouen, 76800 Rouen, France
[b] CEMES-CNRS, 29 rue Jeanne Marvig, 31055, Toulouse, France
[c] Département Matériaux et Mécanique des Composants, EDF R&D, Site des Renardières-Ecuelles, 77818 Moret-sur-Loing cedex, France
[d] LIDEC, Direction Industrielle, EDF DIPNN, 37420 Avoine cedex, France

https://doi.org/10.1016/j.jnucmat.2024.155263

Keywords:
APT
Grain boundary segregation
Thermal ageing
Ion irradiation
Radiation induced/enhanced segregation

A B S T R A C T

Quantitative study of solute segregation phenomenon is crucial in material science. In the present study, the influence of thermal ageing and ion irradiation (both at 400 °C) on intergranular P segregation behaviour was studied by a correlative electron backscattering diffraction (EBSD)/transmission kikuchi diffraction (TKD)/atom probe tomography (APT) methodology. The co-segregation of P, C, Si, Mn, Ni, Cr and Mo appears at grain boundaries (GBs). After both thermal ageing and ion irradiation, there is an increased P segregation for all the detected GB types. The radiation induced/enhanced solute diffusion and segregation mechanisms were also discussed based on thermodynamic and kinetic predictions. The ternary Fe-P-C model overestimates P segregation level in a multicomponent system.

* Corresponding author.
E-mail address: wwwxyxy@163.com (L. Zhang).

1. Introduction

GB segregation issue, in particular the P segregation behaviour at GBs or interfaces, has been intensively studied in the past 70 years [1]. Experimental research was frequently carried out by auger electron spectroscopy (AES), which focuses on some "brittle" GBs from the intergranular fracture surfaces, for instance, in Fe-P [2-4], Fe-P-C [2,5], Fe-Cr-P [2], Ni-Cr [6], Sb-doped Ni-Cr [7], Mn-Ni-Mo [8], Fe-Cr-P-C steels [2] and VVER-1000 welds [9,10]. AES has a fast acquisition speed to collect the data and a good precision on the composition measurement, but the crystallographic information is often missing. In recent years, the correlative transmission electron microscopy (TEM)/APT methodology [11-14] or EBSD/TKD/APT methodology [15-19] offers effective routes to determine a GB's crystallography as well as its chemical nature for non-brittle alloy systems. A correlative TEM/APT approach in a nanocrystalline material has established a C segregation map in relation with GB misorientation angle [11,12]. TKD technique [15,16,20-22] gives a relatively fast and reliable route to obtain a GB's crystallography for polycrystalline materials. APT is a unique technique in quantifying local chemical variations, offering extensive capabilities for both 3D imaging and chemical composition measurements at the atomic scale (interatomic spacing resolution in depth and 0.3∼0.5 nm laterally) [23]. The correlative methodology promotes a better understanding of solute segregation behaviour, which, however, requires both focused ion beam (FIB) lift-out techniques and step-by-step crystallographic characterizations to prepare high quality site-specific specimens containing a GB or an interface [17,18,24,25]. Together with the experiments, computational simulation [26,27] and analytical models [1,28,29] allow thermodynamic parameters of interfacial segregation and the possible segregation mechanisms to be determined.

Intergranular P segregation impairs the atomic bonding [30], thus promoting a change of the brittle fracture mode from transgranular to intergranular [8]. Even at a 0.003 at.% P content, an obvious intergranular P segregation was observed [2]. In a nuclear power plant, low alloy steels suffer from both neutron irradiation and thermal ageing. The long-term safe service of these steels requires a reliable evaluation of the microstructural change and the corresponding property degradation. The non-hardening mechanism, resulting from intergranular P segregation, may significantly contribute to the irradiation embrittlement [9, 31-33]. It was reported that the non-hardening mechanism could contribute to radiation embrittlement of VVER-1000 welds throughout its extended lifetime [9,10,34]. Besides GBs, carbide-ferrite interfaces could also provide effective sites for P segregation [25,34,35]. Under irradiation, the P segregation mechanism could be explained by radiation enhanced segregation (RES) and/or radiation induced segregation (RIS). In the former case, the solute mobility is enhanced by the supersaturated point defects (PDs, including self-interstitials and vacancies), reaching a similar state as under thermal ageing. In the latter case, not only the PD supersaturation is produced, but the fluxes of PDs and solute atoms also move towards the defect sinks such as free surfaces, GBs, dislocations and voids under irradiation. In RIS, the corresponding driving force (dumbbell or vacancy dragging [36-39]) can be purely kinetic and some unpredicted phases may appear in the steels, while the impact of RES is to accelerate the solute segregation towards its equilibrium state. Therefore, it is of critical importance to predict the radiation mechanism.

Our previous research on Fe-P-C model alloys has revealed a RIS mechanism of P and also quantitatively distinguished the role of thermal ageing and ion irradiation on the final P accumulation [40]. While, limited research could be found on the detailed P segregation behaviour for low-alloy steels in relation with GB nature, in which the influence of thermal ageing and irradiation effects should be addressed. Besides, it remains unclear whether the analytical models can describe the P segregation behaviour in practical steels.

Here, we adopted a correlative EBSD/TKD/APT methodology and studied the influence of ageing (thermal ageing and ion irradiation) for different types of GBs in low alloy welds. The quantified GB segregation level was then compared to analytical models.

2. Materials and methods

2.1. Materials, sample preparation and experimental conditions

The studied low-alloy welds have the following chemical composition (in atomic percent): 0.34% C, 0.014% P, 0.84% Si, 1.60% Mn, 0.72% Ni, 0.18% Cr, 0.34% Mo, 0.04% Cu and the balance Fe. As shown in Fig. 1, the reference weld was obtained after submerged arc welding and subsequent stress-relief heat treatment. Then the reference samples were treated in two different routes for comparison: some were ion-irradiated at 400 °C for 2 h and marked as ion-irradiated weld, while some others were thermally-aged at 400 °C for 80000 h and named as thermally-aged weld. A targeted ageing temperature of 400 °C ensures a moderate solute segregation kinetic. Fig. 1 also plots the experimental procedures for ion-irradiated and thermally-aged welds.

Ion irradiation experiments were conducted at the JANNUS facility in Orsay, France. Two thin foils (3 mm in diameter, shown in Fig. S1) were prepared and mounted in the homemade sample holder. A 5 MeV Fe^{3+} beam, a chamber vacuum of 10^{-7} bar, an operation temperature of (400±5) °C, a fluence of 2.85×10^{14} ions/cm^2, a flux of 3.96×10^{10} ions/cm^2/s and a dose rate of 1.3×10^{-5} dpa/s were used. Following ion irradiation, the samples were cooled to 70 °C in vacuum and then depressurized with N_2 cooling to ambient temperature. According to the stopping and range of ions in matter (SRIM) calculation (version SRIM-2013, shown in Fig. 2(a)) using the modified Kinchin-Pease model with a displacement threshold energy of 40 eV [41], it ensures a received dose of about 0.1 dpa in the irradiation depth range 300–600 nm. This dose level equals to a 40 years' operation condition. In this critical depth, there is nearly no influence from implanted ions.

The microstructure was observed by EBSD technique in a dual-beam SEM/FIB instrument (Zeiss XB 540). The EBSD experiments were performed at 20 kV with a working distance of 10 mm. GBs with misorientation characteristics of 60°⟨111⟩ considering a tolerance of 8.7° were considered as Σ3 special HAGB based on the coincidence site lattice (CSL) theory [5] and the Brandon criterion [42]. The detailed site-specific sample preparation using FIB technique, starting from the GB identification in bulk material to the final APT tip containing a specific GB, could be referred in [18]. Besides, special care should be paid to the ion-irradiated weld during sample preparation, ensuring a critical depth of 300–600 nm beneath the irradiation surface for all the studied GBs, as schematically plotted in Fig. 2(b). In practice, the tip with the lift-out chunk was positioned in a manner that the irradiated surface is nearly perpendicular to the SEM view plane, shown in Fig. 2 (c). As exhibited in Fig. 2(c) and (d), the spacing between the final tip apex and the irradiation surface plane can be well controlled to (450 ±150) nm at each step. The location of the GB appearing in the needle is controlled with TKD imaging during the final steps of annular milling, and the analysed GBs locate in the first 100 nm of the final tips.

2.2. Data treatments for crystallography and chemical information

Five parameters are needed to fully describe the GB structure: one for misorientation angle θ, two for rotation axis $\boldsymbol{c} = [h_0k_0l_0]$ and another 2 for the adjacent GB planes $(h_{nA}k_{nA}l_{nA})/(h_{nB}k_{nB}l_{nB})$. Thus, a GB can be described by: $\theta°[h_0k_0l_0](h_{nA}k_{nA}l_{nA})/(h_{nB}k_{nB}l_{nB})$. The identification of the GB character can be referred in [17,18].

A local electrode atom probe (LEAP 4000 XHR, CAMECA) was finally used to do the chemical analysis, with a practical temperature of 55 K, a detection rate of 0.15% and a pulse repetition rate of 200 kHz. Both the commercial IVAS software (CAMECA, v. 3.6.6) and the GPM 3D software (from GPM lab, v. 6.3) were used to do the data reconstruction.

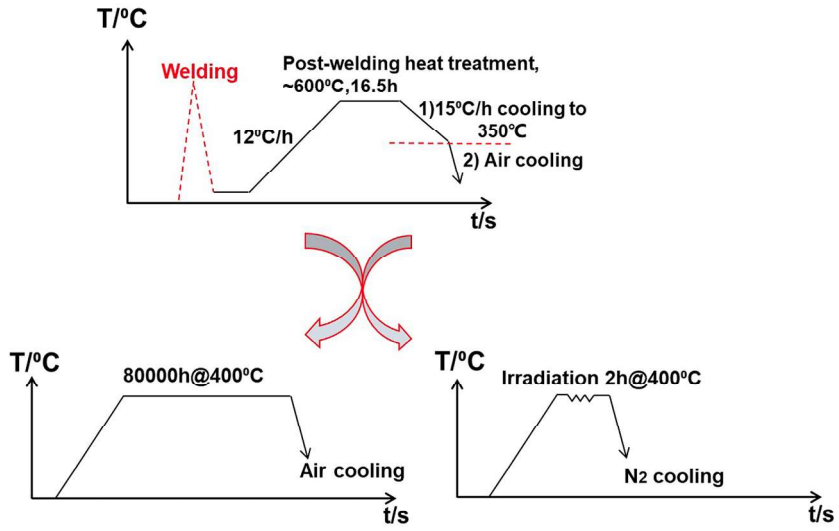

Fig. 1. Schematic illustrations of thermal history for the reference weld, the thermally-aged and the ion-irradiated welds treated at 400 °C.

After APT analysis, the detected ions are exhibited in the form of a mass spectrum. The concentration of an element is calculated from the proportion of detected ions after identifying each isotope and removing the background information. The uncertainty of the measured concentration of element *i*, if considering only the statistical variation, is given by:

$$\sigma_i = \sqrt{\frac{X_i(1-X_i)}{N_{at}}} \tag{1}$$

where X_i is the measured concentration of solute i and N_{at} the total number of atoms in the studied volume. For quantification of intergranular solute segregation level, a general method based on the Gibbsian interfacial excess (Γ_i, in atoms/nm^2) [18,43] was adopted. In the 3D reconstruction map of an APT tip containing a GB, a sampling cylinder perpendicular to the GB is selected to plot cumulative profiles through the GB for each chemical species (referred to Fig. S6 in the Supplementary Document). The Γ_i value is defined as:

$$\Gamma_i = \frac{N_i^{\text{excess}}}{\eta \cdot A} \tag{2}$$

where N_i^{excess} is the number of atoms in excess determined from cumulative profile, η the detection efficiency of the LEAP and A the interfacial area on which the measurement is done. For monolayer P segregation level, we assumed that the segregated P atoms reside in a single close-packed (110) plane of α-iron. This assumption is used for a comparison with the analytical models [1,29,44] and the results from other experimental techniques like AES [8,45,46], in which a narrow segregation region at GB, indicative of a monolayer P segregation, was proposed in steels.

3. Results

3.1. Microstructure evolution

The reference weld has a mixed microstructure of acicular ferrite and intergranular carbides [18], and, in comparison to the "sheaf-like" bainitic ferrite, the acicular ferrite presents a "basket-weave" morphology [47]. After thermal ageing and ion irradiation, the microstructures are exhibited in Fig. 3(a) and (b), respectively, and they are also mainly composed of acicular ferrite grains and intergranular carbides. For most studied regions, these acicular ferrite grain laths are spaced at 1–2.5 μm. The GBs are classified as LAGBs, HAGBs and Σ3 HAGBs. It appears that, for the thermally-aged one (Fig. 3(a)) and the ion-irradiated weld (Fig. 3(b)), there is only a very slight variation of the LAGBs, HAGBs and Σ3 HAGB proportions for the analyzed regions. Since the orientation relationships between parent austenite and acicular ferrite variants are Nishiyama-Wassermann (N-W) and Kurdjumov-Sachs (K-S) [48], our studied GBs are in the misorientation ranges 0–21.5° and 46.5°–60° for all the studied materials. Here, we did not consider the influence of thermal history on the GB type identification of the reference weld. To be exact, the exact primary austenite GBs could not be clearly identified in the studied welds, and this is detailed stated in the Supplementary Document.

The ferrite compositions (especially, C, Mn, Cr and Mo) of the matrix ferrite phase were also quantified by APT experiments. The results are listed in Table 1. The chemical compositions of matrix ferrite remain nearly constant after both thermal ageing and ion irradiation, which suggests that there is probably no carbide evolution after thermal ageing and ion irradiation. Then we focus on the nanoscale solute segregation behaviour.

3.2. Solute segregation behaviour at the studied GBs

Table 2 shows the calculated interfacial excess values of the analysed 17 GBs (4 LAGBs, 7 general HAGBs and 6 Σ3 HAGBs), 7 GBs (2 LAGBs, 2 general HAGBs and 3 Σ3 HAGBs) and 9 GBs (4 LAGBs and 5 general HAGBs) for the reference weld, the thermally-aged weld and the ion-irradiated weld, respectively.

All the studied GBs exhibit a co-segregation of several elements (P, C, Si, Mn, Ni, Cr and Mo), as reported in [9,10,18,44]. No obvious depletion of any chemical species was detected. As an assumption, Si, Cr, Mo, Ni and Mn prefer substitutional segregation while P and C favour interstitial segregation [49,50]. To have a better view, the interfacial excess values of C and P are presented in Fig. 4. In most studied GBs, C has a higher segregation level for the reference, thermally-aged and ion-irradiated welds. This may be due to the fact that C has much higher bulk content than P. The total interfacial excess value of substitutional elements (Si+Cr+Mo+Ni+Mn) is also calculated for each GB and plotted in Fig. 4. It appears that the segregation level of (Si+Cr+Mo+Ni+Mn) is much higher than that of C or P.

4. Discussion

4.1. Inluence of gb character and ageing conditions on solute segregation

Considering the data scattering of solute segregation level within

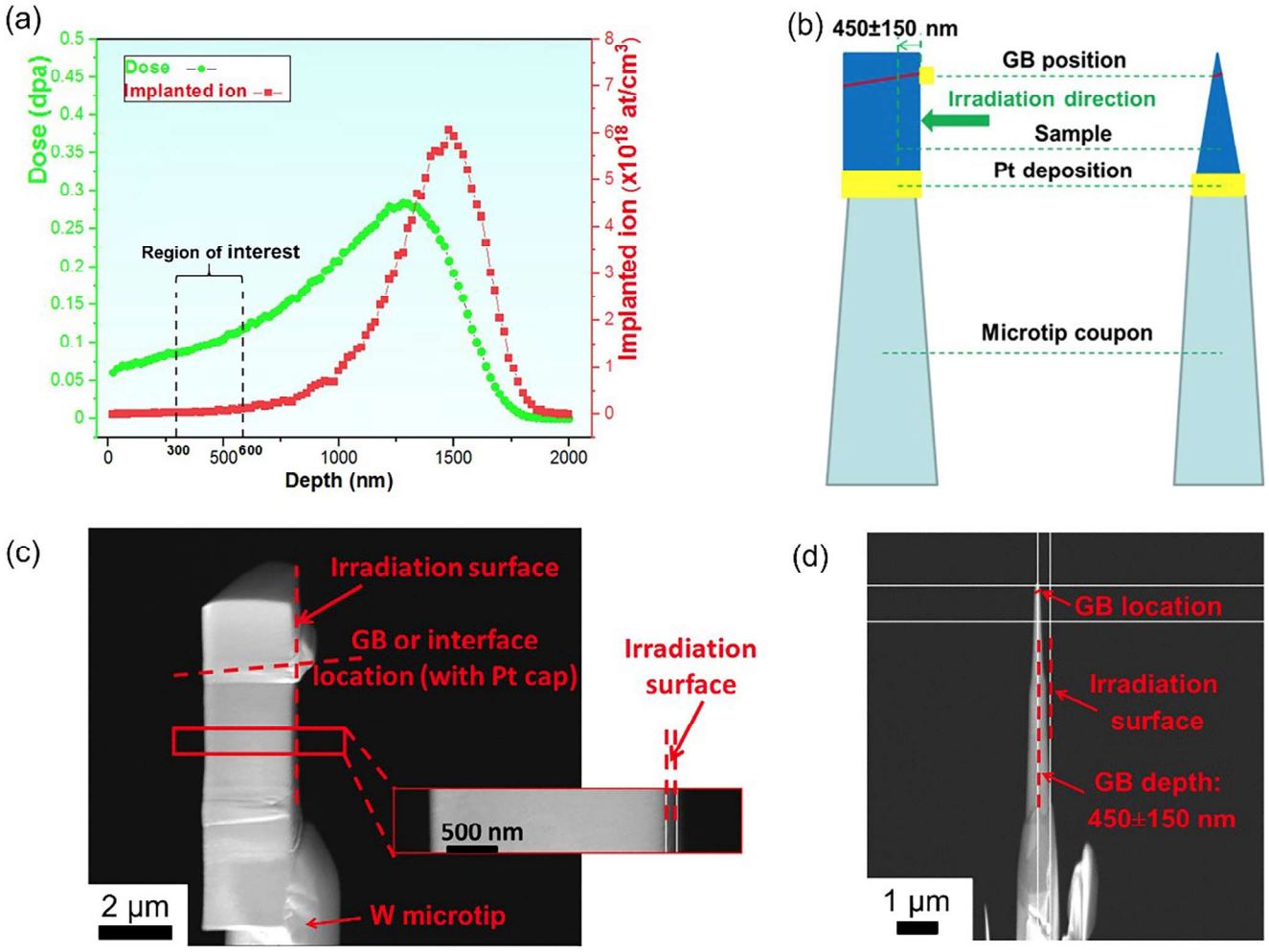

Fig. 2. Illustrations of ion irradiation profiles and FIB-based sample preparation for the ion-irradiated weld. (a) the distribution of dose (green curve) and implanted ion (red curve) as a function of the depth beneath the irradiation surface. (b) the schematic APT sample preparation routes with a specific GB being located at the apex (less than 100 nm) of the thin tip after annular milling. (c) the lift-out chunk (in SEM view) containing a specific GB or a carbide-ferrite interface on a W microtip for the subsequent annular milling. (d) the final tip with the GB being placed within the first 100 nm from the apex. In (a), the 300 to 600 nm depth range is highlighted by dashed dark lines and all the studied GBs were carefully extracted from this region. The irradiation surface planes are particularly placed in order to be nearly perpendicular to the present SEM view planes, with a deviation of less than 100 nm in the local magnification figure of (c). In this case, after careful manipulations during TKD-assisted annular milling, all the identified GBs were finally extracted from a certain irradiation depth (450±150 nm) beneath the irradiation surface.

each GB type (LAGB, Σ3 HAGB or general HAGB), the segregation level is averaged and reported in Table 3.

First, we notice that there is a higher average segregation level in substitutional (Si+Cr+Mo+Ni+Mn) elements than (P + C) elements for all the GB types in the reference, thermally-aged and ion-irradiated welds. Then we discuss the influence of GB character on the solute segregation behaviour. It is clear that the segregated P, C or (P + C) contents are relatively low for all the Σ3 HAGBs. The average (Si+Cr+Mo+Ni+Mn) segregation level is also lower for all the Σ3 HAGBs in comparison to the general HAGBs. The lower segregation levels of both interstitial and substitutional elements suggest the "special" characteristics of Σ3 HAGBs.

Finally, we focus on the P segregation behaviour. Under each condition, the average P segregation level is nearly the same for the studied LAGBs and general HAGBs. Particularly, in the misorientation range 8–15°, each LAGB could share a high P segregation amount as a general HAGB. Here, for an individual GB, no significant P segregation variation was revealed in general HAGBs or the studied LAGBs (misorientation range of 8–15°), especially for the thermally-aged weld or ion-irradiated weld. This differs from previous research that P segregation is lower in LAGBs than HAGBs [4]. In future, more acquired datasets may further clarify the influence of crystallographic orientation on GB segregation (LAGB or HAGB) and also the data scattering in the general HAGBs. After thermal ageing or ion irradiation, there is an increased P segregation for all the GB types (LAGBs, Σ3 HAGBs and general HAGBs). Particularly, P has reached the same segregation level for both thermally-aged and ion-irradiated welds. With a value of 1.8 ± 0.7 atoms/nm^2 (in the thermally-aged weld) or 1.7 ± 0.6 atoms/nm^2 (in the ion-irradiated weld), the average P segregation level is about 3 times after ageing as that of general HAGBs in the reference weld. By contrast, the substitutional (Si+Cr+Mo+Ni+Mn) segregation remains nearly constant after ion irradiation for general HAGBs. Indeed, P segregation appears to reach an equilibrium state after thermal ageing or ion irradiation, which is discussed along with thermodynamic and kinetic considerations.

4.2. *Thermodynamic and kinetic predictions*

The Guttmann's Fe-P-C model was adopted to predict the equilibrium segregation level of P at general HAGBs in Fe matrix at 400°C. The

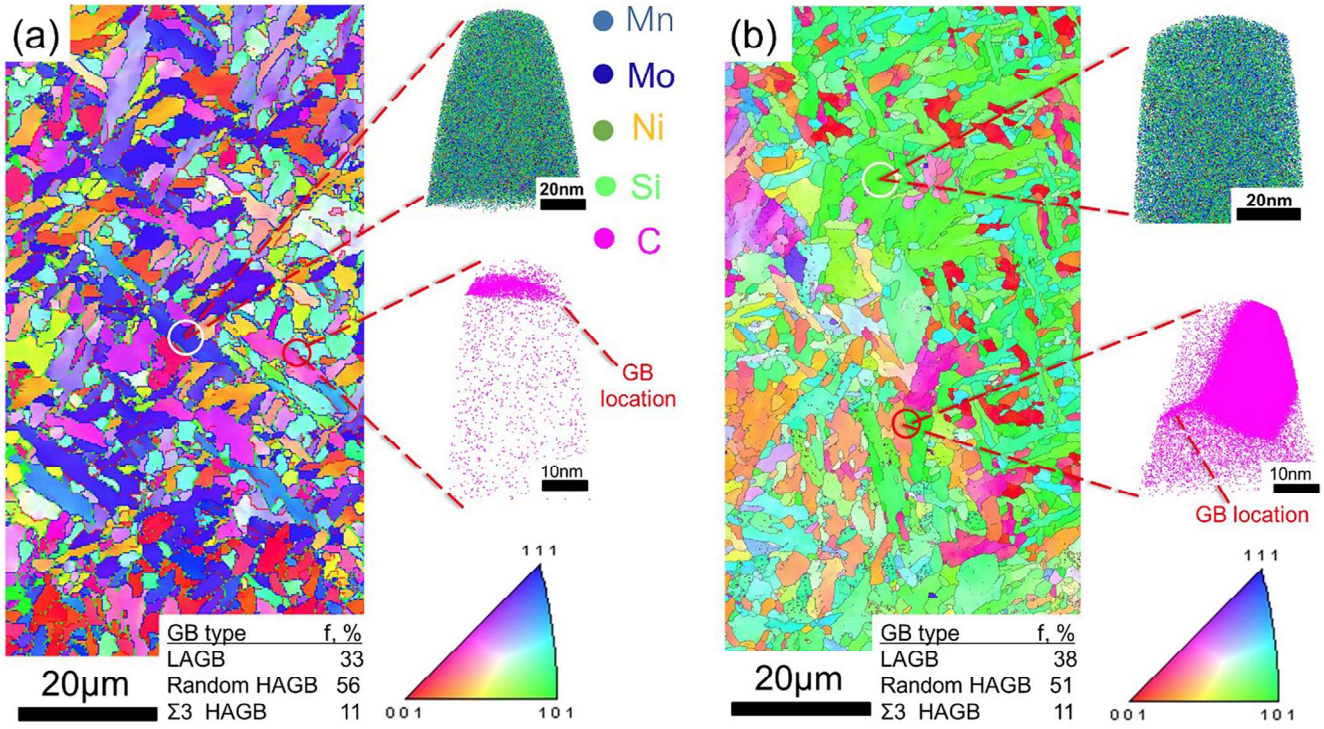

Fig. 3. The microstructures from EBSD and APT characterizations of (a) the thermally-aged weld and (b) the ion-irradiated weld. In both cases, the quantified GB types are inserted, and the 4 reconstructed APT tips were extracted from their respective ferrite matrix and boundary regions (showing the intergranular carbides).

Table 1
Chemical compositions (at.%) of the matrix ferrite under various conditions. The balance element is Fe.

	Reference	Thermally-Aged	Ion-irradiated
C	0.089±0.002	0.081±0.001	0.073±0.001
P	0.016±0.001	0.012±0.001	0.007±0.001
Si	0.843±0.005	0.913±0.004	0.848±0.004
Cr	0.125±0.002	0.161±0.002	0.123±0.001
Mn	1.244±0.006	1.413±0.005	1.283±0.005
Ni	0.761±0.005	0.787±0.004	0.737±0.004
Cu	0.029±0.001	0.029±0.001	0.031±0.001
Mo	0.205±0.003	0.261±0.002	0.176±0.002

equilibrium P segregation at a GB, $C_P^{\varnothing}$, can be written as [1,44]:

$$\frac{C_P^{\varnothing}}{1-C_C^{\varnothing}-C_P^{\varnothing}} = \frac{C_P^{B}}{1-C_C^{B}-C_P^{B}}\exp-\frac{\Delta G_P^{\varnothing}}{RT} \tag{3}$$

in which $C_C^{\varnothing}$, C_P^{B}, C_C^{B} and $\Delta G_P^{\varnothing}$ represent the C segregation level at a GB, the bulk P concentration, the bulk C concentration and the Gibbs free energy, respectively. $\Delta G_i^{\varnothing}$ is a function of the standard segregation enthalpy, $\Delta H_P^{\varnothing}$, and entropy, $\Delta S_P^{\varnothing}$, as expressed below [1]:

$$\Delta G_P^{\varnothing} = \Delta H_P^{\varnothing} - T\Delta S_P^{\varnothing} - 2\alpha_{FeP}\left(C_P^{\varnothing}-C_P^{B}\right) + \alpha_{PC}\left(C_P^{\varnothing}-C_C^{B}\right) \tag{4}$$

in which [1]

$$\Delta H_P^{\varnothing} = \Delta H^{*} + \nu R\left[T\ln C_P^{*}(T)\right] \tag{5}$$

and [51]

$$\Delta S_P^{\varnothing} = \frac{\Delta H_P^{\varnothing}}{T_c} - \sigma_P \tag{6}$$

in which α_{FeP}, α_{PC}, ΔH^{*}, ν, T, $C_P^{*}(T)$, T_c and σ_P are the Fe-P interaction coefficient, the P-C interaction coefficient, the segregation enthalpy at the solubility limit, the non-ideality of binary Fe-based system at the solubility limit, the temperature, the P solubility limit at a certain temperature, the critical temperature for the variation of the segregation enthalpy and entropy with the boundary structure, and the P segregation entropy at a hypothetical boundary with zero enthalpy, respectively.

Kinetically, the dependence of P concentration, $c_P^{\varnothing}(t)$, on time, t, was given by [1]:

$$\frac{C_P^{\varnothing}(t)-C_{P,t=0}^{\varnothing}}{C_P^{\varnothing}-C_{P,t=0}^{\varnothing}} = 1-\exp\left[\frac{4D_P t}{(\beta_P d^{\varnothing})^2}\right]\mathrm{erfc}\left(\frac{2\sqrt{D_P t}}{\beta_P d^{\varnothing}}\right. \tag{7}$$

in which $C_{P,t=0}^{\varnothing}$ is the initial P content at the GB, D_P is the diffusion coefficient of P in matrix, β_P is the enrichment ratio of P at the GB and $d^{\varnothing}$ is the GB thickness. Under irradiation D_P is replaced by D_P^{*}, the radiation-enhanced diffusion coefficient of P in matrix.

Parameters used to calculate the equilibrium GB segregation of P at 400°C and its segregation kinetics could be referred to the literature, in which a ΔH^{*} value of -6 to +2 kJ/mol [1], a $C_{P,t=0}^{\varnothing}$ value of 0.004, a C_C^{B} value of 0.089, a C_P^{B} value of 0.016, a β_P value of 882, a R value of 8.314 J/mol·K, a ν value of 0.82±0.08 [49], a T_c value of 900 K [49], a σ_P value of 54 J/mol·K [49], a α_{PC} value of 7 kJ/mol [1], a α_{FeP} value of 0 [1], a D_P value of 7.5×10^{-21} m^2/s [52], a $T\ln C_P^{*}(T)$ value of -4100 [53] and a $d^{\varnothing}$ value of 0.2 nm [1] were adopted. Taking Faulkner's approach [54], a D_P^{*} value of 9.0×10^{-13} m^2/s was obtained considering a flux of 3.5×10^{10} ions/cm^2/s, a fluence of 2.85×10^{14} ions/cm^2 and a dose rate of 1.3×10^{-5} dpa/s. The radiation-enhanced diffusion coefficient of P was increased by about 10^8 times.

According to the Eqs. (3)-(6), at 400 °C, the predicted equilibrium P segregation level is 0.18±0.03 in monolayer coverage. This value is higher than that of the measured P segregation level, with a monolayer value of 0.11±0.04 (or interfacial excess value of 1.8±0.7 atoms/nm^2), at general HAGBs in thermally-aged weld. According to Eq. (7), the P segregation level as a function of diffusion time during thermal ageing was calculated and plotted in Fig. 5.

As shown in the upper curve in Fig. 5, with the predicted equilibrium value of 0.18, its 90% equilibrium segregation value corresponds to a

Table 2
Interfacial excess values (Γ_i, in atoms/nm^2) of the segregated elements for the studied GBs under different conditions (reference, the thermally-aged and the ion-irradiated).

Element	GB type	P	C	Si	Mn	Ni	Cr	Mo
Reference weld	**LAGB** **5° [6$\bar{5}$2] ($\bar{5}$0$\bar{3}$)/(3$\bar{2}$0)**	0.3 ± 0.2	1.1 ± 0.4	0.28±0.05	2.9 ± 0.2	0.8 ± 0.4	0.20±0.04	1.0 ± 0.3
	LAGB **7° [0$\bar{1}$1] ($\bar{4}$3$\bar{4}$)/($\bar{6}$5$\bar{6}$)**	0.3 ± 0.2	1.3 ± 0.4	0.38±0.06	2.1 ± 0.1	0.8 ± 0.2	–	–
	LAGB **12° [104] (54$\bar{6}$)/(53$\bar{5}$)**	0.9 ± 0.3	1.8 ± 0.9	0.5 ± 0.1	4.8 ± 0.5	1.5 ± 0.8	–	0.6 ± 0.4
	LAGB **12° [$\bar{3}$10] (6$\bar{3}$1)/($\bar{6}$3$\bar{1}$)**	0.5 ± 0.2	2.0 ± 0.7	0.30±0.04	4.0 ± 0.2	1.4 ± 0.7	–	0.9 ± 0.3
	Σ3 HAGB **59° [111] ($\bar{6}$5$\bar{2}$)/($\bar{5}$03)**	0.2 ± 0.1	0.4 ± 0.1	1.3 ± 0.2	4.1 ± 0.3	2.3 ± 0.3	–	0.4 ± 0.2
	Σ3 HAGB **60° [11$\bar{1}$] ($\bar{1}$1$\bar{2}$)/($\bar{3}$10)**	0.2 ± 0.1	1.0 ± 0.6	0.5 ± 0.2	3.2 ± 0.3	1.4 ± 0.7	0.2 ± 0.1	0.5 ± 0.3
	Σ3 HAGB **60° [343] ($\bar{4}$41)/($\bar{4}$1$\bar{5}$)**	0.3 ± 0.2	1.8 ± 0.6	2.1 ± 0.3	5.3 ± 0.4	1.3 ± 0.3	–	0.6 ± 0.4
	Σ3 HAGB **59.5° [11$\bar{1}$] (4$\bar{1}$1)/($\bar{5}$22)**	0.3 ± 0.2	0.8 ± 0.6	1.4 ± 0.2	6.5 ± 0.7	–	–	0.3 ± 0.2
	Σ3 HAGB **60° [111] (101)/(01$\bar{1}$)**	0.07±0.06	1.2 ± 0.4	0.34±0.03	3.5 ± 0.1	0.5 ± 0.3	0.4 ± 0.1	0.7 ± 0.2
	Σ3 HAGB **60° [443] (45$\bar{1}$)/(103)**	0.4 ± 02	1.2 ± 0.6	0.8 ± 0.1	4.0 ± 0.2	0.8 ± 0.4	0.2 ± 0.1	0.6 ± 0.2
	General HAGB **52° [$\bar{1}$01] (6$\bar{1}$5)/(25$\bar{3}$)**	0.4 ± 0.2	4.6 ± 1.2	–	6.5 ± 0.4	2.0 ± 0.5	0.3 ± 0.1	3.4 ± 1.5
	General HAGB **49° [403] (010)/(35$\bar{5}$)**	0.6 ± 0.3	5.0 ± 1.2	0.5 ± 0.1	5.8 ± 0.3	1.1 ± 0.5	0.3 ± 0.1	1.8 ± 0.9
	General HAGB **49.5° [$\bar{1}$10] ($\bar{4}$2$\bar{5}$)/(5$\bar{4}$2)**	0.3 ± 0.1	4.1 ± 1.4	1.3 ± 0.2	7.1 ± 0.4	–	0.5 ± 0.2	1.7 ± 0.9
	General HAGB **54° [2$\bar{4}$3] (1$\bar{1}$0)/(1$\bar{5}$0)**	1.0 ± 0.5	3.7 ± 1.0	0.8 ± 0.1	5.6 ± 0.5	0.8 ± 0.4	–	1.4 ± 1.0
	General HAGB **52° [$\bar{3}$3$\bar{1}$] ($\bar{5}$43)/(65$\bar{5}$)**	0.8 ± 0.2	5.3 ± 1.1	1.9 ± 0.2	6.6 ± 0.3	1.8 ± 0.9	0.4 ± 0.1	2.8 ± 1.0
	General HAGB **54° [$\bar{5}$25] ($\bar{1}$1$\bar{2}$)(0$\bar{3}$1)**	0.11±0.02	6.7 ± 1.6	–	1.7 ± 0.1	–	0.4 ± 0.1	1.5 ± 0.4
	General HAGB **54° [433] (5$\bar{5}$2)/(6$\bar{3}$1)**	0.9 ± 0.3	3.3 ± 0.9	0.54±0.07	4.8 ± 0.3	1.7 ± 1.0	0.3 ± 0.1	2.7 ± 0.7
80000h@400 °C	**LAGB** **8° [1$\bar{1}$1] ($\bar{6}$2$\bar{5}$)/(5$\bar{5}$2)**	1.9 ± 0.5	1.8 ± 0.6	0.30±0.01	6.4 ± 0.5	2.7 ± 1.3	0.09±0.04	1.3 ± 0.5
	LAGB **14° [41$\bar{4}$] (01$\bar{3}$)/(0$\bar{1}$0)**	1.5 ± 0.3	2.5 ± 0.7	1.6 ± 0.2	8.0 ± 0.3	3.7 ± 1.9	0.2 ± 0.1	1.3 ± 0.3
	General HAGB **55° [3$\bar{2}$3] ($\bar{6}$4$\bar{5}$)/(501)**	2.0 ± 0.7	1.6 ± 0.9	2.4 ± 0.5	8.9 ± 0.8	4.1 ± 2.5	–	0.6 ± 0.4
	General HAGB **56° [$\bar{1}$10] (1$\bar{3}$2)/(3$\bar{1}$4)**	1.6 ± 0.7	3.0 ± 1.5	3.0 ± 0.4	10.5 ± 0.9	3.9 ± 2.0	0.7 ± 0.3	1.7 ± 0.9
	Σ3 HAGB **59° [1$\bar{1}$1] ($\bar{2}$01)/($\bar{1}$02)**	0.6 ± 0.4	0.4 ± 0.3	0.9 ± 0.2	3.7 ± 0.3	1.5 ± 0.7	–	0.2 ± 0.1
	Σ3 HAGB **60° [- 11] (143)/(216)**	0.7 ± 0.3	0.7 ± 0.4	0.7 ± 0.1	5.1 ± 0.4	1.5 ± 0.8	–	0.9 ± 0.5
	Σ3 HAGB **59° [11$\bar{1}$] (3$\bar{4}$1)/(145)**	1.0 ± 0.4	0.3 ± 0.2	1.3 ± 0.1	4.8 ± 0.3	3.3 ± 1.4	0.13±0.04	0.2 ± 0.1
Irradiation @ 400 °C)	**LAGB** **12° [100] (124)/(6$\bar{2}$1)**	2.3 ± 0.5	1.8 ± 0.6	0.8 ± 0.1	3.3 ± 0.2	3.6 ± 1.8	–	0.6 ± 0.2
	LAGB **12° [104] (33$\bar{2}$)/($\bar{1}$3$\bar{1}$)**	1.1 ± 0.4	5.6 ± 1.5	1 ± 0.2	3.7 ± 0.3	1.9 ± 1.1	0.4 ± 0.2	2.7 ± 0.7
	LAGB **12° [320] ($\bar{1}$6$\bar{3}$)/(1$\bar{2}$6)**	2.5 ± 0.4	0.7 ± 0.1	1.4 ± 0.1	2.3 ± 0.1	3.2 ± 1.6	0.2 ± 0.1	0.3 ± 0.1
	LAGB **14° [41$\bar{2}$] ($\bar{5}$36)/(66$\bar{5}$)**	2.8 ± 1.4	4.0 ± 2.0	1.3 ± 0.2	5.7 ± 0.6	4.3 ± 2.6	0.4 ± 0.2	1.8 ± 0.9
	General HAGB **51° [22$\bar{1}$] (2$\bar{5}$0)/($\bar{6}$3$\bar{5}$)**	3.7 ± 1.5	6.0 ± 3.7	–	8.0 ± 0.9	3.8 ± 1.6	0.2 ± 0.1	1.9 ± 0.9
	General HAGB **60° [5$\bar{2}$5] (04$\bar{5}$)/($\bar{1}$4$\bar{6}$)**	1.9 ± 0.7	4 ± 1.8	0.44±0.05	3.8 ± 0.3	2.3 ± 1.2	–	2.4 ± 0.8
	General HAGB **60° [5$\bar{2}$5] ($\bar{6}$5$\bar{1}$)/($\bar{5}$40)**	1.0 ± 0.2	3.3 ± 0.9	–	3.3 ± 0.2	1.2 ± 0.7	0.4 ± 0.2	2.5 ± 0.7
	General HAGB **52.5° [$\bar{2}$23] ($\bar{1}$6$\bar{4}$)/(5$\bar{2}$0)**	1.5 ± 0.4	2.5 ± 0.5	1.5 ± 0.1	3.6 ± 0.2	2.7 ± 1.3	0.3 ± 0.1	1.3 ± 0.4
	General HAGB **52° [101] (5$\bar{6}$3)/(641)**	0.5 ± 0.4	4.0 ± 2.6	–	3.7 ± 0.6	3.1 ± 1.9	0.21±0.06	0.9 ± 0.5

Notes: "-" means that no clear segregation or depletion is detected.

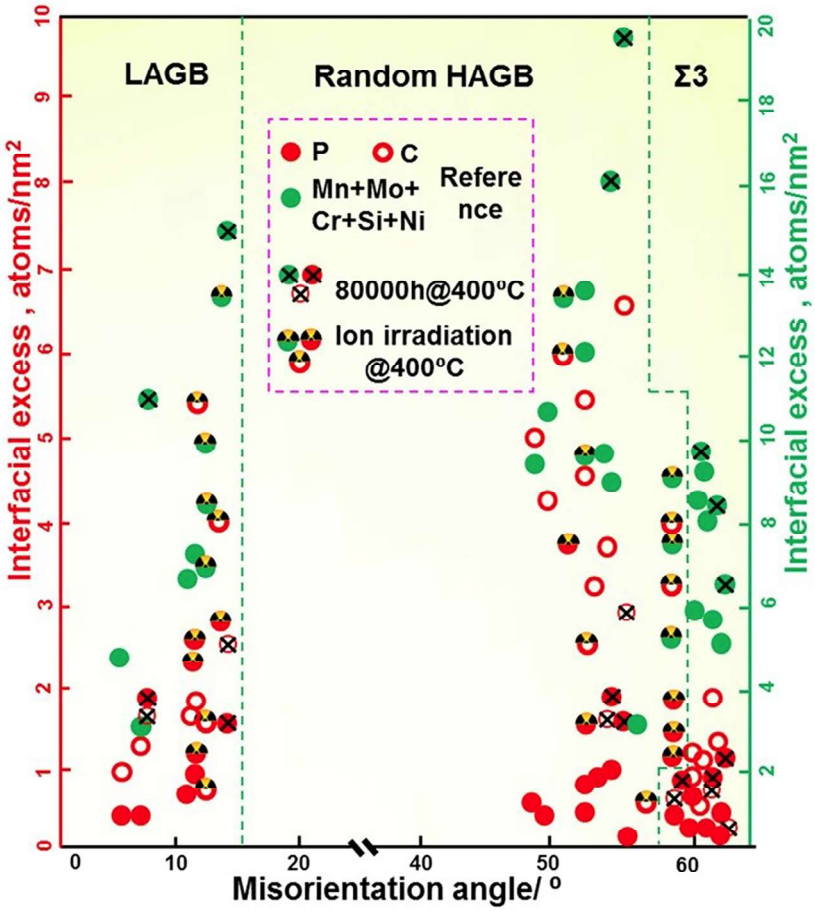

Fig. 4. Plot of interfacial excess values of P, C and (Si+Cr+Mo+Ni+Mn) for all the identified GBs under different conditions (reference, thermal ageing and ion irradiation).

Table 3
The average interfacial excess values (Γ_i, in atoms/nm^2) of segregants (P, C, P + C and Si+Ni+Mn+Cr+Mo) for the identified GBs under different conditions (reference, thermal ageing and ion irradiation). For each type of GB, the number of investigated features is given into parenthesis.

	GB type	Γ_P	Γ_C	$\Gamma_{(P+C)}$	$\Gamma_{(Si+Cr+Mo+Ni+Mn)}$
Reference	**LAGBs (4)**	0.5 ± 0.2	1.6 ± 0.6	2.1 ± 0.8	5.8 ± 1.3
	General HAGBs (7)	**0.6 ± 0.2**	**4.7 ± 1.3**	**5.3 ± 1.5**	**9.7 ± 1.9**
	Σ3 HAGBs (6)	0.2 ± 0.1	1.1 ± 0.5	1.3 ± 0.6	7.2 ± 1.1
Thermally-aged (80,000 h @400 °C)	**LAGBs (2)**	1.7 ± 0.4	2.3 ± 1.1	4.0 ± 1.5	12.8 ± 2.6
	General HAGBs (2)	**1.8 ± 0.7**	**2.2 ± 0.7**	**4.0 ± 1.4**	**17.9 ± 4.4**
	Σ3 HAGBs (3)	0.8 ± 0.4	0.5 ± 0.3	1.3 ± 0.7	8.1 ± 1.7
Ion-irradiated (400 °C)	**LAGBs (4)**	2.2 ± 0.7	3.0 ± 1.1	5.2 ± 1.8	9.7 ± 2.8
	General HAGBs (5)	**1.7 ± 0.6**	**4.0 ± 1.9**	**5.7 ± 2.5**	**9.5 ± 2.6**

time period of 54077 h. Or, if using the experimental segregation level of 0.11, 11668 h is required to reach the 90% equilibrium segregation value (the bottom curve in Fig. 5). It is suggested that P has probably reached its equilibrium segregation state after thermal ageing at 400 °C for 80000 h. For ion-irradiated weld, P seems to require only several seconds to reach its equilibrium state at 400 °C according to Eq. (5) adopting a D_P^* value. Along with the fact that the P segregation level (for the studied LAGBs and general HAGBs) is nearly the same after irradiation as that of the thermally-aged one, it is suggested that P may have reach the same equilibrium segregation state for both thermally-aged and ion-irradiated welds at 400 °C. Consequently, a radiation induced equilibrium segregation, or RES mechanism, could be responsible for the P segregation behaviour in the ion-irradiated weld. This is different from the RIS-dominated mechanism reported for some high-dose irradiated materials [39,55-58]. Under ion irradiation, no clear secondary phases or solute rich clusters were observed in the studied welds. P segregation kinetics is accelerated due to supersaturated PDs under irradiation, however, the mobile complexes of PDs and P atoms are low and the RIS mechanism may be not favored in the multicomponent system. Besides, these PDs may also prefer high mutual recombination during migration in comparison to their annihilation at PD sinks. More detailed discussions on the segregation mechanism, including solute-PD complex model as well as the inverse Kirkendall model [59,60], could be made based on extensive experimental results of binary or ternary alloys under different irradiation conditions.

Thermodynamically, the ternary Fe-P-C model seems to predict a higher equilibrium segregation level than the experimental one. This may be attributed to the presence of other alloying elements. The absolute value of Gibbs free energy, $\Delta G_P^{\varnothing c}$, decreases when the material complexity increases, which may give an overestimation of equilibrium P segregation level in such a multicomponent system. Another possible explanation is that, during data curation for average monolayer P

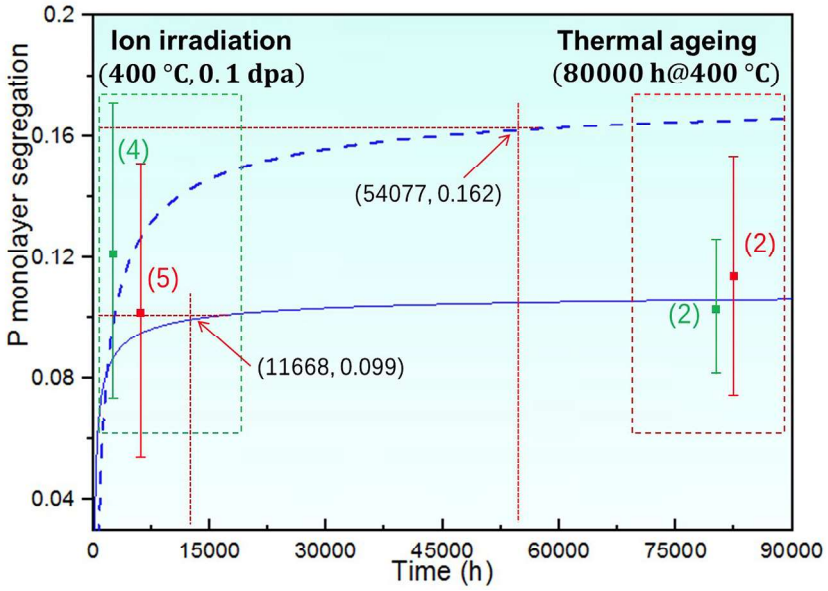

Fig. 5. Predictions of intergranular P segregation kinetics as a function of time for the thermally-aged weld (80000h@400 °C). Note that, the 90% equilibrium segregation value, corresponding to a time of 54077 h (or 11668 h) using an equilibrium segregation level of 0.18 from Fe-P-C model (or 0.11 from APT analysis) is plotted in the upper dashed (or bottom solid) curve. For a better comparison between thermal ageing and ion irradiation, the average P segregation values for measured 2 LAGBs (or 4 LAGBs) and 2 general HAGBs (or 5 general HAGBs) in thermally-aged weld (or ion-irradiated weld), are marked in green and red, respectively.

segregation, we assumed that the segregated P atoms reside in a single close-packed (110) plane of a BCC α-iron, underestimating its monolayer segregation level.

Besides, we have also performed a detailed estimation of equilibrium P segregation based on binary Fe-P, ternary Fe-P-C and multicomponent models for the reference weld, as reported in the Supplementary Document. We calculated the corresponding segregation levels of P, considering its segregation at both interstitial and substitutional sites. It is revealed that the Fe-P-C ternary model gives a better estimation (but also higher than the experimental value), and that the predicted segregation value is also strongly affected by the interaction coefficients in the multicomponent model. Further research requires careful investigations on the attractive or repulsive interactions amongst alloying elements.

5. Conclusion

In the present work, the intergranular solute segregation phenomena were quantitatively studied by a correlative EBSD/TKD/APT methodology in low-alloy steel welds under different conditions, including reference weld, thermal ageing at 400 °C for 80000 h and ion irradiation at 400 °C with a dose of about 0.1 dpa. Main conclusions can be made as follows:

(1) The co-segregation of P, C, Si, Mn, Ni, Cr and Mo appears at all the studied GBs, amongst which Σ3 HAGBs present lower interstitial segregation than general HAGBs. Considering that Si, Cr, Mo, Ni and Mn prefer substitutional segregation while P and C favour interstitial segregation, there is a higher average segregation level in substitutional (Si+Cr+Mo+Ni+Mn) elements than (P + C) elements for all the GB types in the reference, thermally-aged and ion-irradiated welds.

(2) In the present work, under each condition (reference, thermal ageing or ion irradiation), the studied LAGBs and general HAGBs share the equivalent average P segregation level. Particularly, in the misorientation range 8–15°, each LAGB could share a high P segregation amount as a general HAGB. In future, more research on P distribution across different types of GB is required to draw final conclusions. After thermal ageing at 400 °C for 80000 h or ion irradiation at 400 °C, there is an increased average P segregation for all the studied GB types (LAGBs, Σ3 HAGBs and general HAGBs).

(3) Thermodynamic and kinetic calculations seem to reveal a RES mechanism of P under ion irradiation, in which P has reached the same equilibrium segregation state as that after thermal ageing at 400 °C. Ternary Fe-P-C model overestimates equilibrium P segregation level than experimental results.

CRediT authorship contribution statement

Leifeng Zhang: Writing – review & editing, Writing – original draft, Visualization, Methodology, Investigation, Formal analysis, Data curation, Conceptualization. **Bertrand Radiguet:** Writing – review & editing, Supervision, Resources, Methodology, Funding acquisition, Conceptualization. **Patrick Todeschini:** Writing – review & editing, Validation, Resources, Funding acquisition. **Christophe Domain:** Writing – review & editing, Validation, Funding acquisition. **Yang Shen:** Writing – review & editing, Resources. **Philippe Pareige:** Writing – review & editing, Supervision, Resources, Funding acquisition, Conceptualization.

Declaration of competing interest

The authors declare that they have no known competing financial interests or personal relationships that could have appeared to influence the work reported in this paper.

Data availability

Data will be made available on request.

Acknowledgement

This work was performed on the GENESIS platform, financially supported by Centre National de la Recherche Scientifique (CNRS)

belonging to the project entitled “Investissements d’avenir” with a reference number ANR-11-EQPX-0020. This work is part of the EM2VM Joint Laboratory Study and modeling of the Microstructure for Ageing of Materials. This work was supported by the MAI-sn (Materials Ageing Institute-Scientific Network, http://themai.org/scientific-network).

Supplementary materials

Supplementary material associated with this article can be found, in the online version, at doi:10.1016/j.jnucmat.2024.155263.

References

[1] P. Lejcek, Grain Boundary Segregation in Metals, Springer Science & Business Media, Berlin, 2010.
[2] H. Erhart, H.J. Grabke, Equilibrium segregation of phosphorus at grain boundaries of Fe–P, Fe-C-P, Fe-Cr-P, and Fe-Cr-C-P alloys, Met. Sci. 15 (9) (1981) 401–408.
[3] S. Suzuki, K. Abiko, H. Kimura, Phosphorus segregation related to the grain boundary structure in an Fe-P alloy, Scripta Metall. Mater. 15 (10) (1981) 1139–1143.
[4] C. Li, D.B. Williams, Anisotropy of P grain boundary segregation in a rapidly solidified Fe-0.6 wt% P alloy, Interface Sci 11 (2003) 461–472.
[5] G.O. Williams, V. Randle, J.R. Cowan, P. Spellward, The role of misorientation and phosphorus content on grain growth and intergranular fracture in iron-carbon-phosphorus alloys, J. Microsc. 213 (3) (2004) 321–327.
[6] T. Ogura, C.J. McMahon, H.C. Feng, V. Vitek, Structure-dependent intergranular segregation of phosphorus in austenite in a Ni-Cr steel, Acta Metall. Mater. 26 (9) (1978) 1317–1330.
[7] J. Kameda, C.J. McMahon, Solute segregation and brittle fracture in an alloy steel, Metall. Mater. Trans. A 11 (1) (1980) 91–101.
[8] C. Naudin, J.M. Frund, A. Pineau, Intergranular fracture stress and phosphorus grain boundary segregation of a Mn-Ni-Mo steel, Scripta Mater 40 (9) (1999) 1013–1019.
[9] E.A. Kuleshova, B.A. Gurovich, Z.V. Lavrukhina, D.A. Maltsev, S.V. Fedotova, A. S. Frolov, G.M. Zhuchkov, Study of the flux effect nature for VVER-1000 RPV welds with high nickel content, J. Nucl. Mater. 483 (2017) 1–12.
[10] S.V. Fedotova, E.A. Kuleshova, D.A. Maltsev, M.A. Saltykov, Complex study of grain boundary segregation in long-term irradiated reactor pressure vessel steels, J. Nucl. Mater. 528 (2020) 151865.
[11] M. Herbig, D. Raabe, Y.J. Li, P. Choi, S. Zaefferer, S. Goto, Atomic-scale quantification of grain boundary segregation in nanocrystalline material, Phys. Rev. Lett. 112 (12) (2014) 126103.
[12] D. Raabe, M. Herbig, S. Sandlöbes, Y. Li, D. Tytko, M. Kuzmina, D. Ponge, P. Choi, Grain boundary segregation engineering in metallic alloys: a pathway to the design of interfaces, Curr. Opin. Solid St. M. 18 (4) (2014) 253–261.
[13] A.K. Da Silva, G. Leyson, M. Kuzmina, D. Ponge, M. Herbig, S. Sandlöbes, B. Gault, J. Neugebauer, D. Raabe, Confined chemical and structural states at dislocations in Fe-9wt% Mn steels: a correlative TEM-atom probe study combined with multiscale modelling, Acta Mater 124 (2017) 305–315.
[14] A. Gupta, X. Zhou, G.B. Thompson, G.J. Tucker, Role of grain boundary character and its evolution on interfacial solute segregation behavior in nanocrystalline Ni-P, Acta Mater 190 (2020) 113–123.
[15] K. Babinsky, R. De Kloe, H. Clemens, S. Primig, A novel approach for site-specific atom probe specimen preparation by focused ion beam and transmission electron backscatter diffraction, Ultramicroscopy 144 (2014) 9–18.
[16] K. Babinsky, W. Knabl, A. Lorich, R. De Kloe, H. Clemens, S. Primig, Grain boundary study of technically pure molybdenum by combining APT and TKD, Ultramicroscopy 159 (2015) 445–451.
[17] A. Akhatova, F. Christien, V. Barnier, B. Radiguet, E. Cadel, F. Cuvilly, P. Pareige, Investigation of the dependence of phosphorus segregation on grain boundary structure in Fe-PC alloy: cross comparison between Atom Probe Tomography and Auger Electron Spectroscopy, Appl. Surf. Sci. 463 (2019) 203–210.
[18] L. Zhang, B. Radiguet, P. Todeschini, C. Domain, Y. Shen, P. Pareige, Investigation of solute segregation behavior using a correlative EBSD/TKD/APT methodology in a 16MND5 weld, J. Nucl. Mater. 523 (2019) 434–443.
[19] S. Baik, M.J. Olszta, S.M. Bruemmer, D.N. Seidman, Grain-boundary structure and segregation behavior in a nickel-base stainless alloy, Scripta Mater 66 (10) (2012) 809–812.
[20] G.C. Sneddon, P.W. Trimby, J.M. Cairney, Transmission Kikuchi diffraction in a scanning electron microscope: a review, Mater. Sci. Eng. R 110 (2016) 1–12.
[21] B.M. Jenkins, J.O. Douglas, H.M. Gardner, D. Tweddle, A. Kareer, P.S. Karamched, N. Riddle, J.M. Hyde, P.A. Bagot, G.R. Odette, A more holistic characterisation of internal interfaces in a variety of materials via complementary use of transmission Kikuchi diffraction and Atom probe tomography, Appl. Surf. Sci. 528 (2020) 147011.
[22] D. Tweddle, P. Hamer, Z. Shen, V.P. Markevich, M.P. Moody, P.R. Wilshaw, Direct observation of hydrogen at defects in multicrystalline silicon, Prog. Photovolt. Res. Appl. 29 (11) (2021) 1–7.
[23] M.K. Miller, R.G. Forbes, Atom-probe tomography: the Local Electrode Atom Probe, Springer Science & Business Media, New York, 2014.
[24] M. Herbig, Spatially correlated electron microscopy and atom probe tomography: current possibilities and future perspectives, Scripta Mater 148 (2018) 98–105.
[25] L. Zhang, B. Radiguet, P. Todeschini, C. Domain, Y. Shen, P. Pareige, Study of solute segregation behavior at carbide–ferrite interfaces in 16MND5 welds, J. Nucl. Mater. 542 (2020) 152531.
[26] L. Messina, M. Nastar, T. Garnier, C. Domain, P. Olsson, Exact ab initio transport coefficients in bcc Fe-X (X= Cr, Cu, Mn, Ni, P, Si) dilute alloys, Phys. Rev. B 90 (10) (2014) 104203.
[27] C. Domain, C. Becquart, Solute - <111>interstitial loop interaction in α-Fe: a DFT study, J. Nucl. Mater. 499 (2018) 582–594.
[28] M. Guttmann, Equilibrium segregation in a ternary solution: a model for temper embrittlement, Surf. Sci. 53 (1) (1975) 213–227.
[29] P. Lejček, M. Šob, V. Paidar, Interfacial segregation and grain boundary embrittlement: an overview and critical assessment of experimental data and calculated results, Prog. Mater. Sci. 87 (2017) 83–139.
[30] M. Hashimoto, Y. Ishida, R. Yamamoto, M. Doyama, Atomistic studies of grain boundary segregation in Fe-P and Fe-B alloys - I. Atomic structure and stress distribution, Acta Metall. Mater. 32 (1) (1984) 1–11.
[31] B.A. Gurovich, E.A. Kuleshova, Y.A. Nikolaev, Y.I. Shtrombakh, Assessment of relative contributions from different mechanisms to radiation embrittlement of reactor pressure vessel steels, J. Nucl. Mater. 246 (2–3) (1997) 91–120.
[32] B.A. Gurovich, E.A. Kuleshova, Y.I. Shtrombakh, O.O. Zabusov, E.A. Krasikov, Intergranular and intragranular phosphorus segregation in Russian pressure vessel steels due to neutron irradiation, J. Nucl. Mater. 279 (2–3) (2000) 259–272.
[33] E.A. Kuleshova, B.A. Gurovich, Z.V. Lavrukhina, M.A. Saltykov, S.V. Fedotova, A. N. Khodan, Assessment of segregation kinetics in water-moderated reactors pressure vessel steels under long-term operation, J. Nucl. Mater. 477 (2016) 110–122.
[34] Y.I. Shtrombakh, B.A. Gurovich, E.A. Kuleshova, D.A. Maltsev, S.V. Fedotova, A. A. Chernobaeva, Thermal ageing mechanisms of VVER-1000 reactor pressure vessel steels, J. Nucl. Mater. 452 (1–3) (2014) 348–358.
[35] B. Gurovich, E. Kuleshova, O. Zabusov, S. Fedotova, A. Frolov, M. Saltykov, D. Maltsev, Influence of structural parameters on the tendency of VVER-1000 reactor pressure vessel steel to temper embrittlement, J. Nucl. Mater. 435 (1–3) (2013) 25–31.
[36] A.A. Vasiliev, V.V. Rybin, A.A. Zisman, The nature of the phosphorus atom mobility in bcc iron irradiated at low temperatures, J. Nucl. Mater. 231 (1996) 249–253.
[37] C. Domain, C.S. Becquart, Ab initio calculations of defects in Fe and dilute Fe-Cu alloys, Phys. Rev. B 65 (2001) 24103.
[38] E. Meslin, C. Fu, A. Barbu, F. Gao, F. Willaime, Theoretical study of atomic transport via interstitials in dilute Fe-P alloys, Phys. Rev. B 75 (2007) 94303.
[39] B. Gómez-Ferrer, C. Heintze, C. Pareige, On the role of Ni, Si and P on the nanostructural evolution of FeCr alloys under irradiation, J. Nucl. Mater. 517 (2019) 35–44.
[40] A. Akhatova, Méthodologie instrumentale à l’échelle atomique pour une meilleure compréhension des mécanismes de ségrégation intergranulaire dans les aciers: application au phosphore, PhD thesis, Université de Rouen Normandie, 2017.
[41] ASTM, Standard Practice for Neutron Radiation Damage Simulation by Charged-Particle Irradiation, West Conshohocken, E521-96 (2009).
[42] D.G. Brandon, The structure of high-angle grain boundaries, Acta Metall. Mater. 14 (1966) 1479–1484.
[43] B.W. Krakauer, D.N. Seidman, Absolute atomic-scale measurements of the Gibbsian interfacial excess of solute at internal interfaces, Phys. Rev. B 48 (9) (1993) 6724–6727.
[44] M. Guttmann, P. Dumoulin, M. Wayman, The thermodynamics of interactive co-segregation of phosphorus and alloying elements in iron and temper-brittle steels, Metall. Trans. A 13 (10) (1982) 1693–1711.
[45] W. Phythian, C. English, Microstructural evolution in reactor pressure vessel steels, J. Nucl. Mater. 205 (1993) 162–177.
[46] P. Lejček, Characterization of grain boundary segregation in an Fe-Si alloy, Anal. Chim. Acta 297 (1–2) (1994) 165–178.
[47] R. Farrar, P. Harrison, Acicular ferrite in carbon-manganese weld metals: an overview, J. Mater. Sci. 22 (1987) 3812–3820.
[48] S. Babu, H. Bhadeshia, Stress and the acicular ferrite transformation, Mater. Sci. Eng. A - Struct. 156 (1992) 1–9.
[49] P. Lejček, S. Hofmann, Interstitial and substitutional solute segregation at individual grain boundaries of α-iron: data revisited, J. Phys. Condens. Mat. 28 (6) (2016) 64001.
[50] P. Lejček, S. Hofmann, Modeling grain boundary segregation by prediction of all the necessary parameters, Acta Mater 170 (2019) 253–267.
[51] P. Lejček, S. Hofmann, J. Janovec, Prediction of enthalpy and entropy of solute segregation at individual grain boundaries of α-iron and ferrite steels, Mater. Sci. Eng. A - Struct. 462 (2007) 76–85.
[52] S.G. Druce, G. Gage, G. Jordan, Effect of ageing on properties of pressure vessel steels, Acta Metall. Mater. 34 (4) (1986) 641–652.
[53] P. Lejček, S. Hofmann, Grain boundary segregation diagrams of α-iron, Interface Sci 2 (1) (1993) 163–174.
[54] R.G. Faulkner, S. Song, P.E.J. Flewitt, M. Victoria, P. Marmy, Grain boundary segregation under neutron irradiation in dilute alloys, J. Nucl. Mater. 255 (1998) 189–209.
[55] Z. Jiao, G.S. Was, Novel features of radiation-induced segregation and radiation-induced precipitation in austenitic stainless steels, Acta Mater 59 (2011) 1220–1238.
[56] A.J. Ardell, P. Bellon, Radiation-induced solute segregation in metallic alloys, Curr. Opin. Solid St. M. 20 (2016) 115–139.

[57] C. Pareige, V. Kuksenko, P. Pareige, Behaviour of P, Si, Ni impurities and Cr in self ion irradiated Fe–Cr alloys–Comparison to neutron irradiation, J. Nucl. Mater. 456 (2015) 471–476.
[58] B. Gómez-Ferrer, C. Dethloff, E. Gaganidze, L. Malerba, C. Hatzoglou, C. Pareige, Nano-hardening features in high-dose neutron irradiated Eurofer97 revealed by atom-probe tomography, J. Nucl. Mater. 537 (2020) 152228.
[59] J.P. Wharry, Z. Jiao, G.S. Was, Application of the inverse Kirkendall model of radiation-induced segregation to ferritic–martensitic alloys, J. Nucl. Mater. 425 (2012) 117–124.
[60] J.P. Wharry, G.S. Was, The mechanism of radiation-induced segregation in ferritic–martensitic alloys, Acta Mater 65 (2014) 42–55.